

Topological valley Hall polariton condensation

Authors: Kai Peng^{1,2,3†}, Wei Li^{1,3†}, Meng Sun^{4†}, Jose D. H. Rivero^{5,6}, Chaoyang Ti⁷, Xu Han⁷, Li Ge^{5,6}, Lan Yang⁸, Xiang Zhang^{2*}, and Wei Bao^{1,3*}

Affiliations:

¹Department of Materials Science and Engineering, Rensselaer Polytechnic Institute, Troy, New York, USA

²Nanoscale Science and Engineering Center, University of California, Berkeley, California, USA

³Department of Electrical and Computer Engineering, University of Nebraska-Lincoln, Lincoln, Nebraska, USA

⁴Faculty of Science, Beijing University of Technology, Beijing, China

⁵Department of Physics and Astronomy, College of Staten Island, CUNY, Staten Island, New York, USA

⁶The Graduate Center, CUNY, New York, New York, USA

⁷Center for Nanoscale Materials, Argonne National Laboratory, Lemont, Illinois, USA

⁸Department of Electrical and Systems Engineering, Washington University, St Louis, Missouri, USA

†These authors contributed equally to this work.

*Corresponding authors. Email: baow2@rpi.edu (W.B.) or xiang@berkeley.edu (X.Z.)

1 **Abstract:**

2 Topological insulator is a novel state of matter featuring robust directional propagation and
3 immunity to defect perturbations of the edge/surface state. Exciton-polaritons, i.e., the hybrid
4 quasiparticles of exciton and photon in semiconductor microcavities, have been proposed as a
5 tunable nonlinear platform for emulating topological phenomena. However, the construction of
6 topological propagating edge states with exciton-polariton condensation remains elusive in
7 experiments, mainly due to excitonic material restrictions. Here, we overcome this challenge by
8 using the emergent excitonic halide perovskite material with a valley Hall lattice design and
9 unambiguously demonstrate the first topological propagating edge state with polariton
10 condensation. This is achieved at room temperature without any external magnetic field. A large
11 topological bandgap was observed, and across the critical pumping density, the topologically
12 protected interfacial edge states exhibit strong nonlinear polariton condensation with clear long-
13 range spatial coherence. Our result provides a new active nonlinear many-body photonic system
14 with flexible light-matter composition and tunable inter-quasiparticle interactions for studying
15 topological phenomena and novel phases of condensed matter.

1 Topological insulators, initially introduced in the two-dimensional (2D) electron gas system
2 under a magnetic field ¹, elucidate a remarkable material state of insulating in bulk but conducting
3 on edge ². These edges are formed at the interfaces where the spatial areas with different
4 topological invariants meet. The fundamental principle of topological invariance protects the
5 unimpeded flow of electrons along the edges without dissipation and back-scattering by non-
6 magnetic impurities and disorders. This visionary concept has been adopted by other systems, such
7 as cold atoms ³, acoustics ^{4,5}, and photonics ⁶⁻¹⁰, and has led to many groundbreaking insights into
8 topological physics.

9 Recently, cavity exciton-polaritons, due to the part-light part-matter nature, were theoretically
10 proposed to be a distinct nonlinear system with tunable quasiparticle composition and interparticle
11 interactions as a powerful platform to emulate the topological phenomena ¹¹⁻¹⁴. In a semiconductor
12 microcavity, exciton-polaritons are formed in the strong coupling regime where the coupling rate
13 between exciton and cavity photon is much faster than each dissipation rate. These bosonic
14 exciton-polaritons carry small effective mass inherited from their photonic component and strong
15 nonlinearity inherited from their excitonic component, enabling a nonlinear Bose-Einstein
16 condensation (BEC) process (referred to as polariton condensation) at much-elevated temperatures
17 compared to the cold atom systems ¹⁵⁻¹⁷. In contrast to creating lattice potential via laser
18 interference in cold atoms, one can construct almost arbitrary periodic potentials in polariton
19 lattices via nanofabrication, enabling complete band structures and coupling strengths tunning
20 among these atom-like polariton condensates ^{18,19}. Besides, in the polariton platform, one can
21 directly visualize the band structures and edge state propagations in studying topological models,
22 which can only be indirectly evidenced in cold atoms. Compared to a pure noninteractive photonic
23 system in the weak coupling regime, the interactive exciton component of the quasiparticles
24 provides unique tunability of polariton-polariton interactions and opportunities to independently

control the exciton and its interactions via external gauge fields ^{12,13,20,21}. Although efforts with various material platforms have been made to study the linear ^{22–24} and nonlinear ^{25–27} topological polaritons, they either cannot enter the nonlinear condensation regime or only show localized dot-like condensation in one-dimensional (1D) Su-Schrieffer-Heeger (SSH) models. Thus, a nonlinear polariton platform that can support the most prominent feature of topological insulators, such as robust propagating modes against sharp-turn corners or various defects, remains elusive. This restricts the research for developing close analogs of topological condensed matter systems in polariton systems.

Semiconducting lead halide perovskites have recently emerged as a new polaritonic platform at room temperature ^{28–33}, showing excellent performances and offering new opportunities in topological polaritonics. However, due to the in-plane optical birefringence ^{33,34}, polariton lattices with 2D topological interfaces can not be constructed with the most mature CsPbBr_3 materials.

In this work, we overcome these challenges and present the first experimental construction of topologically protected propagating modes with polariton condensation. This is achieved by adopting a valley Hall topological insulator lattices and utilizing the isotropic excitonic halide perovskites CsPbCl_3 materials. Inspired by the van der Waals valleytronic materials, valley Hall photonic topological insulator has a valley degree of freedom due to the breaking lattice inversion symmetry and can host topological edge states without an external magnetic field or the construction of photonic pseudospins ^{35,36}. By integrating topological valley Hall insulator design and high-quality isotropic excitonic halide perovskites, we have fabricated large and uniform valley Hall polariton lattice and successfully observed topological propagating edge states within a bandgap of 18.8 meV. These edge states exhibit robust transport along the topological interface, encountering sharp turns at the corners of the structures. More importantly, across the critical

1 pumping density, we observed the strong nonlinear polariton condensation of the topologically
2 protected edge states. Interference experiments reveal global phase-locking of the polariton
3 condensates across the entire closed topological interface due to the non-zero polariton in-plane
4 propagation momentum, acting as a coherent topological polariton laser array with low threshold.
5 Our work provides a new active nonlinear many-body polaritonic platform with tunable light-
6 matter composition and unique interparticle interaction for the study of topological phenomena. It
7 also paves the way for future inversionless topological laser arrays in the strong coupling regime.

8 **Topological polariton valley Hall design and realization**

9 In our experiment, we utilized perovskite CsPbCl_3 microcavities, which consist of a large-size
10 single crystal CsPbCl_3 plate and a polymethyl methacrylate (PMMA) spacer sandwiched between
11 top and bottom distributed Bragg reflectors (DBR), as shown in Fig. 1a. Previous works based on
12 CsPbBr_3 cannot achieve propagating topological edge mode because of the optical birefringence
13 ^{33,34}. In contrast, the CsPbCl_3 crystal has an in-plane isotropic refractive index ²⁹ and was chosen
14 in our experiments to construct the homogenous potential landscape before the PMMA patterning.
15 We emphasize this homogenous landscape is required in most 2D topological propagating edge
16 states (described in Fig. S4). However, due to the low solubility of precursors for Cl-based halide
17 perovskites and the limitation of CVD methods, growing large CsPbCl_3 thin-film-like single
18 crystals has been quite a challenge. To address this, we carefully modified our growth procedures
19 (see Materials and Methods for details) and finally produced thin single-crystalline perovskites
20 with large lateral sizes through either solution synthesis in nanocavity or CVD. With these
21 excellent crystal samples (Fig. 2a), we then fabricated polariton lattices by patterning the PMMA
22 spacer with standard electron-beam lithography (EBL) on top of the perovskite ³¹. A top DBR
23 plate was finally dry-transferred onto the PMMA pattern to form a vertical cavity. Further

information on sample fabrication and characterization can be found in the Methods and Extended Data Fig. 1-2. The typical Q-factor of the cavity is approximately 400-700 (relatively low, due to the limited reflectivity of DBR mirror at short wavelength), depending on the thickness and homogeneity of the cavities. The samples show strong coupling between the excitons and the cavity photons with a Rabi splitting of \sim 280 meV, as shown in Extended Data Fig. 5 of unpatterned samples. The transversely patterned PMMA spacer induced a deep periodic potential of up to \sim 150 meV, which confines the polaritons in the regions covered by PMMA. The CsPbCl₃ also has excellent stability and preserves high optical excitonic quality during the fabrications with treatments such as O₂ plasma and EBL PMMA development in MIBK/IPA solution (Extended Data Fig. 3).

The structure of the polaritonic valley Hall insulator is utilized to create topologically protected edge states. Valley Hall insulators break the spatial inversion symmetry to achieve valley degrees of freedom without a magnetic field^{35,36}. This property has attracted significant interest in photonics and acoustics to achieve robust waveguide propagation^{5,37,38} and electrically pumped terahertz topological lasers at low temperatures³⁹. This design has also been theoretically proposed in the interacting bosonic quantum fluids (such as polariton condensates) to achieve the topologically protected transport of chiral vortex⁴⁰. Here, we constructed a lattice structure consisting of quasi-hexagonal holes patterned on a PMMA spacer, which breaks the inversion symmetry of the perfect hexagonal holes and leads to the opening of a bandgap at the Dirac points (K and K') at the corners of the Brillouin zone³⁵. This design is more fabrication-friendly for EBL patterning and topologically equivalent to the coupled micropillars usually used in the research of polariton lattices, as shown in Fig. S3. These gaps have opposite valley Chern numbers of $\pm 1/2$, making them topologically distinct (described in Supplementary Text Section II and Fig. S1 and S2). By introducing a boundary between domains with opposite hexagonal hole directions, we

1 created a topological interface with edge states. Numerical simulation (described in Supplementary
2 Text Section I) shows the edge states (solid red dots) within the bandgap along the interface
3 direction ($K \rightarrow \Gamma \rightarrow K'$ direction along the x-axis) in Fig. 1b. Figure 1c shows the real-space
4 polariton distribution of the topologically protected edge state, which reveals that the continuous
5 mode remains robust even with a 120° sharp corner.

6 Figure 2a displays a typical well-transferred CsPbCl_3 plate on a bottom DBR substrate. The
7 large size of the sample enables us to fabricate a uniform 2D polariton lattice with sufficient
8 periods and high excitonic quality. The scanning electron microscope (SEM) image of a typical
9 sample after EBL patterning is shown in Fig. 2b. The topological interface indicated by yellow
10 dashed lines is formed at the domains where opposite hexagonal hole directions meet. The lattice
11 constant is $1.2 \mu\text{m}$, and the short and long sides of the hexagonal holes are 0.27 and $0.73 \mu\text{m}$,
12 respectively. In Fig. 2d, the momentum-space (k-space) PL spectra of the bulk area along the
13 $K \rightarrow \Gamma \rightarrow K'$ direction (parallel to the topological interface direction) with non-resonant excitation
14 is presented, which matches well with the simulations shown in Fig. 2c. Notably, a large bandgap
15 of 18.8 meV can be clearly observed above the ground state band. In contrast, when we excite the
16 interface, an edge band marked by red arrows appears within the bandgap in Fig. 2e, in excellent
17 agreement with the simulations presented in Fig. 1b.

18 The topological valley Hall effect also has shown potential in photonic waveguides with
19 robust signal transport^{37,38}. In our perovskite exciton-polariton system, we explored the polariton
20 propagation along a waveguide structure as illustrated in Fig. 2f. A non-resonant excitation laser
21 spot (indicated by dashed red circles in Fig. 2f) was used in pumping the topological interface. The
22 PL of the edge states was filtered out using a 1-nm bandwidth filter, and the saturated image is
23 shown in Fig. 2f-II. Clearly, the topological edge states are propagating in two directions along the

1 interface with intrinsic polariton decay, even with three sharp 120° turns, and the small
2 inhomogeneity of the sample does not affect the robustness of their propagation. Comparatively,
3 the bulk state diffuses undirectly, and the trivial edge state has substantial loss encountering 120°
4 sharp corners due to the lack of topological protection, as demonstrated in Extended Data Fig. 8.
5 These different propagations are also proved by the time-dependent numerical simulations
6 (described in Supplementary Text Section III and Supplementary Videos S1-S3). These results
7 demonstrate the potential of valley Hall design for the future applications of polaritonic
8 waveguides and switches.

9 **Polariton condensation of valley Hall states**

10 The nonlinear character of the perovskite exciton-polariton enables us to enter the room-
11 temperature polariton condensation regime of the topological edge states, which share closer
12 analogies with topological condensed matter systems. Polaritons are driven-dissipative non-
13 equilibrium systems, allowing them to condensate into excited or ground states simply by tuning
14 the right gain and loss. To achieve polariton condensation into the topological edge states, we
15 chose an exciton-photon detuning of ~ -110 meV to favor polariton relaxation into the edge states.
16 Samples with a closed equilateral triangular boundary of 10 periods (along each edge) were
17 fabricated. A 370-nm, 250-fs pulsed laser shaped with a spatial light modulator was utilized to
18 pump the triangle's edges non-resonantly. Figure 3d shows the real-space PL emissions of the
19 sample at low pumping power. Here, the triangular topological edges can be clearly identified. A
20 feedback mechanism was employed to adjust the pumping laser profile and facilitate uniform PL
21 emissions of the triangular topological interface (Methods and Extended Data Fig. 4)⁴¹.

22 Polariton condensation can be observed by performing k-space PL dispersion measurements
23 at increasing pump powers, as displayed in Fig. 3a-I-IV. Specifically, k-space PL images of the

same sample in Fig. 2d-e are given at 0.05, 0.5, 1, and 1.5 times the condensation threshold (P_{th}) pumping power, where P_{th} is approximately $15.2 \mu\text{J cm}^{-2}$. To properly extract the PL emission in these plots only from one edge of the triangular edges for the polariton dispersion measurements in Fig. 3a, we used a pinhole at the imaging plane to select only the region enclosed by the red dashed circle in Fig. 3d-e (see Extended Data Fig. 4 for details). As the pumping power increases, clearly nonlinear increase in PL intensity and the narrowing of the linewidth of the edge state can be observed, indicating the occurrence of polariton condensation as shown in Fig. 3b. And at 1.5 P_{th} , the system fully condensates at the topological edge states at $k_x = \pm 2.6 \mu\text{m}^{-1}$, as shown in Fig. 3a-IV. Moreover, the real-space image in Fig. 3e unambiguously shows that the condensation occurs only at the triangular interface, providing solid evidence of the topological polariton condensation behavior of the edge states.

The repulsive interaction of polaritons, which originates from the exciton component, leads to a continuous blueshift of the topological edge mode, a crucial signature of the polariton condensation. Below the condensation threshold, the primary interaction between polaritons and the exciton reservoir caused a stronger blueshift compared to after the threshold, as demonstrated in Fig. 3c. Noticeably, the blueshift induced by polariton-polariton interactions in the topological edge states is more substantial than in the bulk state due to the spatial selective pumping and the localization of polaritons along the topological edge. As shown in Fig. 3a, the energy gap between the topological edge band (marked as red arrows) and the ground bulk state (marked as orange arrows) at $k_x = 0$ increases with increasing pumping power. To the best of our knowledge, this dynamic tuning of the topological energy band is uniquely associated with the strong coupling polariton systems. Moreover, it potentially provides a new degree of control for the nonlinear and non-Hermitian topological states ^{34,42-46}.

The non-zero in-plane momentum of the polariton condensates also allows the polariton quantum fluid to flow along the topological interface, which could lead to a global phase-locking of the condensates along the entire edge. To confirm this, we overlapped the real-space image in Fig. 3e with its mirror image using a Michelson interferometer, as shown in Fig. 3f. The interference fringes observed along the entire triangle edge unambiguously justify the long-range spatial phase coherence of the topological condensates. This characteristic also makes the whole topological edges act as a single coherent vertical emitting polariton laser source ⁴⁷. In contrast, the condensation of trivial bulk states cannot achieve global phase-locking like the topological edge states due to the lack of propagation characteristics, as shown in Extended Data Fig. 10. Our work also presents a larger vertical emitting topological laser array of up to 60 laser emitters (60 triangles on the interface) with a much lower threshold based on a strongly coupled polaritonic system at room temperature, compared to previous studies on topological laser arrays with 30 emitters (30 pillars) using III-V quantum dots weak-coupling photonic systems at low temperatures ⁴⁸. Additionally, the use of a standard EBL patterned PMMA spacer on top of the perovskite layer allowed us to avoid the difficult deep etching of the thick DBRs layers in III-V quantum well and quantum dots structures, resulting in better homogeneity in emission profile along the topological edge. Moreover, the spatial coherence of the emitters along the topological edge originates from the in-plane propagation of the topological edge states. Therefore, defects and inhomogeneities, in general, will not compromise coherence to build up along the topological polariton condensation edges, as they typically cannot fully block the in-plane propagation of the modes. This feature was also illustrated in experiments with another sample, as shown in Extended Data Fig. 9.

More samples were fabricated to investigate the condensation coherence of topological edge states in Fig. 4. The condensation of the sample in Fig. 4a-I exhibits more pronounced interference

1 fringes at zero time delay, indicating better spatial coherent performance. The fringe visibility, i.e.,
2 g_1 coherence, was extracted in Fig. 4b. Strong spatial coherence along the whole topological
3 interface of the triangle is clearly observed, suggesting global phase-locking. Furthermore, the
4 temporal coherence was also measured by tuning the delay time. The interference fringe amplitude
5 weakens with the increase of delay time, as shown in Fig. 4a-I-III. The extracted maximum g_1 is
6 shown in Fig. 4c. The excellent spatial and temporal coherence proves the condensation of the
7 whole topological edge states in our perovskite microcavity.

8 This topological-protected valley Hall insulator configuration can also be extended to more
9 intricate geometries with multiple sharp corners. To illustrate this, we fabricated two additional
10 geometries resembling fish-like topological edges with open and closed mouths, as shown in Fig.
11 5. Remarkably, once the condensation threshold is surpassed, the systems exhibit a uniform
12 condensation at the topological interfaces, as demonstrated clearly in Fig. 5b and 5d. These
13 compelling results underscore the versatility of our platform, allowing for the investigation of
14 topological phenomena and the utilization of topological polariton laser arrays across a broad
15 spectrum of geometries ^{49,50}.

16 Discussion and Conclusion

17 It is worth noting that previous works of topological Chern insulators based on the 2D GaAs
18 at low temperatures offer strong topological resilience to defects and disorder theoretically, but
19 require a strong magnetic field to break time-reversal symmetry and open a tiny topological
20 bandgap of only ~ 0.1 meV ²⁶. Therefore, the ultra-small bandgap cannot support condensation at
21 the topological edge state, due to the polariton linewidth (~ 0.1 meV - 0.5 meV) and polariton
22 blueshift (~ 1 meV). Consequently, only a trivial bulk state condensation outside the bandgap was
23 shown. In contrast, valley Hall design lacks broken time-reversal symmetry and can only offer

1 topological protection to defects that respect the symmetry of the lattice (120° sharp corners)⁵¹.
2 Nevertheless, in our CsPbCl₃ perovskite system at room temperature, almost arbitrary large-scale
3 potential landscaping can be constructed, and a substantial topological bandgap (18.8 meV in our
4 experiment) can be easily opened, enabling the condensation to occur precisely at the pure
5 topological 2D edge states.

6 To conclude, we report the first polariton condensation of the topologically protected
7 propagating edge states. Our work establishes a room-temperature polariton platform capable of
8 constructing large-scale condensation lattices with arbitrary potential landscapes for emulating
9 topological physics and exploring potential new phases of quantum matter, which were previously
10 inaccessible with low-temperature GaAs and 2D van der Waals materials systems. The driven-
11 dissipation non-equilibrium and interacting quantum fluid characteristics of polaritons also make
12 them suitable for studying non-Hermitian topological physics. Moreover, our system can also be
13 extended to the chiral perovskite ⁵² or 2D materials ^{22,53} for helical polaritons and many other
14 exciting topological designs ⁵⁴, such as quantum spin Hall insulators ^{22,23,55,56}, to manipulate the
15 spin and chiral propagating topological condensations. The low threshold presented in our work
16 also paves the way for electrically pumped polariton lasers ^{57,58} and inversionless coherent
17 topological polariton laser arrays and for future technology applications at room temperature.

1 **References:**

- 2 1. Klitzing, K. v., Dorda, G. & Pepper, M. New Method for High-Accuracy Determination
3 of the Fine-Structure Constant Based on Quantized Hall Resistance. *Phys. Rev. Lett.* **45**,
4 494–497 (1980).
- 5 2. Hasan, M. Z. & Kane, C. L. Colloquium: Topological insulators. *Rev. Mod. Phys.* **82**,
6 3045–3067 (2010).
- 7 3. Cooper, N. R., Dalibard, J. & Spielman, I. B. Topological bands for ultracold atoms. *Rev.*
8 *Mod. Phys.* **91**, 15005 (2019).
- 9 4. Yang, Z. *et al.* Topological Acoustics. *Phys. Rev. Lett.* **114**, 114301 (2015).
- 10 5. Lu, J. *et al.* Observation of topological valley transport of sound in sonic crystals. *Nat.*
11 *Phys.* **13**, 369–374 (2017).
- 12 6. Haldane, F. D. M. & Raghu, S. Possible Realization of Directional Optical Waveguides in
13 Photonic Crystals with Broken Time-Reversal Symmetry. *Phys. Rev. Lett.* **100**, 13904
14 (2008).
- 15 7. Wang, Z., Chong, Y., Joannopoulos, J. D. & Soljačić, M. Observation of unidirectional
16 backscattering-immune topological electromagnetic states. *Nature* **461**, 772–775 (2009).
- 17 8. Khanikaev, A. B. *et al.* Photonic topological insulators. *Nat. Mater.* **12**, 233–239 (2013).
- 18 9. Lu, L., Joannopoulos, J. D. & Soljačić, M. Topological photonics. *Nat. Photonics* **8**, 821–
19 829 (2014).
- 20 10. Ozawa, T. *et al.* Topological photonics. *Rev. Mod. Phys.* **91**, 15006 (2019).
- 21 11. Karzig, T., Bardyn, C.-E., Lindner, N. H. & Refael, G. Topological Polaritons. *Phys. Rev.*
22 *X* **5**, 31001 (2015).
- 23 12. Bardyn, C.-E., Karzig, T., Refael, G. & Liew, T. C. H. Topological polaritons and
24 excitons in garden-variety systems. *Phys. Rev. B* **91**, 161413 (2015).
- 25 13. Nalitov, A. V., Solnyshkov, D. D. & Malpuech, G. Polariton Z Topological Insulator.
26 *Phys. Rev. Lett.* **114**, 116401 (2015).
- 27 14. Kartashov, Y. V & Skryabin, D. V. Two-Dimensional Topological Polariton Laser. *Phys.*
28 *Rev. Lett.* **122**, 83902 (2019).
- 29 15. Deng, H., Weihs, G., Santori, C., Bloch, J. & Yamamoto, Y. Condensation of
30 semiconductor microcavity exciton polaritons. *Science* **298**, 199–202 (2002).
- 31 16. Kasprzak, J. *et al.* Bose-Einstein condensation of exciton polaritons. *Nature* **443**, 409–414
32 (2006).
- 33 17. Deng, H., Haug, H. & Yamamoto, Y. Exciton-polariton Bose-Einstein condensation. *Rev.*
34 *Mod. Phys.* **82**, 1489–1537 (2010).
- 35 18. Kim, N. Y. *et al.* Dynamical d-wave condensation of exciton–polaritons in a two-
36 dimensional square-lattice potential. *Nat. Phys.* **7**, 681–686 (2011).
- 37 19. Jacqmin, T. *et al.* Direct Observation of Dirac Cones and a Flatband in a Honeycomb
38 Lattice for Polaritons. *Phys. Rev. Lett.* **112**, 116402 (2014).

1 20. Cristofolini, P. *et al.* Coupling Quantum Tunneling with Cavity Photons. *Science* **336**,
2 704–707 (2012).

3 21. Tsintzos, S. I. *et al.* Electrical Tuning of Nonlinearities in Exciton-Polariton Condensates.
4 *Phys. Rev. Lett.* **121**, 37401 (2018).

5 22. Liu, W. *et al.* Generation of helical topological exciton-polaritons. *Science* **370**, 600–604
6 (2020).

7 23. Li, M. *et al.* Experimental observation of topological Z2 exciton-polaritons in transition
8 metal dichalcogenide monolayers. *Nat. Commun.* **12**, 4425 (2021).

9 24. Guddala, S. *et al.* Topological phonon-polariton funneling in midinfrared metasurfaces.
10 *Science* **374**, 225–227 (2021).

11 25. St-Jean, P. *et al.* Lasing in topological edge states of a one-dimensional lattice. *Nat.*
12 *Photonics* **11**, 651–656 (2017).

13 26. Klembt, S. *et al.* Exciton-polariton topological insulator. *Nature* **562**, 552–556 (2018).

14 27. Dusel, M. *et al.* Room-Temperature Topological Polariton Laser in an Organic Lattice.
15 *Nano Lett.* **21**, 6398–6405 (2021).

16 28. Su, R. *et al.* Perovskite semiconductors for room-temperature exciton-polaritonics. *Nat.*
17 *Mater.* **2021** **20**, 1315–1324 (2021).

18 29. Su, R. *et al.* Room-Temperature Polariton Lasing in All-Inorganic Perovskite
19 Nanoplatelets. *Nano Lett.* **17**, 3982–3988 (2017).

20 30. Peng, K. *et al.* Room-temperature polariton quantum fluids in halide perovskites. *Nat.*
21 *Commun.* **13**, 7388 (2022).

22 31. Su, R. *et al.* Observation of exciton polariton condensation in a perovskite lattice at room
23 temperature. *Nat. Phys.* **16**, 301–306 (2020).

24 32. Łempicka-Mirek, K. *et al.* Electrically tunable Berry curvature and strong light-matter
25 coupling in liquid crystal microcavities with 2D perovskite. *Sci. Adv.* **8**, eabq7533 (2023).

26 33. Tao, R. *et al.* Halide perovskites enable polaritonic XY spin Hamiltonian at room
27 temperature. *Nat. Mater.* **21**, 761–766 (2022).

28 34. Rui, S. *et al.* Direct measurement of a non-Hermitian topological invariant in a hybrid
29 light-matter system. *Sci. Adv.* **7**, eabj8905 (2022).

30 35. Ma, T. & Shvets, G. All-Si valley-Hall photonic topological insulator. *New J. Phys.* **18**,
31 025012 (2016).

32 36. Dong, J.-W., Chen, X.-D., Zhu, H., Wang, Y. & Zhang, X. Valley photonic crystals for
33 control of spin and topology. *Nat. Mater.* **16**, 298–302 (2017).

34 37. Shalaev, M. I., Walasik, W., Tsukernik, A., Xu, Y. & Litchinitser, N. M. Robust
35 topologically protected transport in photonic crystals at telecommunication wavelengths.
36 *Nat. Nanotechnol.* **14**, 31–34 (2019).

37 38. He, X.-T. *et al.* A silicon-on-insulator slab for topological valley transport. *Nat. Commun.*
38 **10**, 872 (2019).

39 39. Zeng, Y. *et al.* Electrically pumped topological laser with valley edge modes. *Nature* **578**,

1 246–250 (2020).

2 40. Bleu, O., Malpuech, G. & Solnyshkov, D. D. Robust quantum valley Hall effect for
3 vortices in an interacting bosonic quantum fluid. *Nat. Commun.* **9**, 3991 (2018).

4 41. Töpfer, J. D. *et al.* Engineering spatial coherence in lattices of polariton condensates.
5 *Optica* **8**, 106–113 (2021).

6 42. Gao, T. *et al.* Observation of non-Hermitian degeneracies in a chaotic exciton-polariton
7 billiard. *Nature* **526**, 554–558 (2015).

8 43. Pernet, N. *et al.* Gap solitons in a one-dimensional driven-dissipative topological lattice.
9 *Nat. Phys.* **18**, 678–684 (2022).

10 44. Zhao, H. *et al.* Non-Hermitian topological light steering. *Science* **365**, 1163–1166 (2019).

11 45. Solnyshkov, D. D. *et al.* Microcavity polaritons for topological photonics [Invited]. *Opt.*
12 *Mater. Express* **11**, 1119–1142 (2021).

13 46. Ardizzone, V. *et al.* Polariton Bose–Einstein condensate from a bound state in the
14 continuum. *Nature* **605**, 447–452 (2022).

15 47. Kavokin, A. *et al.* Polariton condensates for classical and quantum computing. *Nat. Rev.*
16 *Phys.* **4**, 435–451 (2022).

17 48. Dikopoltsev, A. *et al.* Topological insulator vertical-cavity laser array. *Science* **373**, 1514–
18 1517 (2021).

19 49. Bahari, B. *et al.* Nonreciprocal lasing in topological cavities of arbitrary geometries.
20 *Science* **358**, 636–640 (2017).

21 50. Bandres, M. A. *et al.* Topological insulator laser: Experiments. *Science* **359**, eaar4005
22 (2018).

23 51. Rosiek, C. A. *et al.* Observation of strong backscattering in valley-Hall photonic
24 topological interface modes. *Nat. Photonics* **17**, 386–392 (2023).

25 52. Long, G. *et al.* Chiral-perovskite optoelectronics. *Nat. Rev. Mater.* **5**, 423–439 (2020).

26 53. Lundt, N. *et al.* Optical valley Hall effect for highly valley-coherent exciton-polaritons in
27 an atomically thin semiconductor. *Nat. Nanotechnol.* **14**, 770–775 (2019).

28 54. Berestennikov, A. S. *et al.* Enhanced Photoluminescence of Halide Perovskite
29 Nanocrystals Mediated by a Higher-Order Topological Metasurface. *J. Phys. Chem. C*
30 **125**, 9884–9890 (2021).

31 55. Wu, L.-H. & Hu, X. Scheme for Achieving a Topological Photonic Crystal by Using
32 Dielectric Material. *Phys. Rev. Lett.* **114**, 223901 (2015).

33 56. Berestennikov, A. *et al.* Perovskite Microlaser Integration with Metasurface Supporting
34 Topological Waveguiding. *ACS Nano* **17**, 4445–4452 (2023).

35 57. Schneider, C. *et al.* An electrically pumped polariton laser. *Nature* **497**, 348–352 (2013).

36 58. Suchomel, H. *et al.* Platform for Electrically Pumped Polariton Simulators and
37 Topological Lasers. *Phys. Rev. Lett.* **121**, 257402 (2018).

38

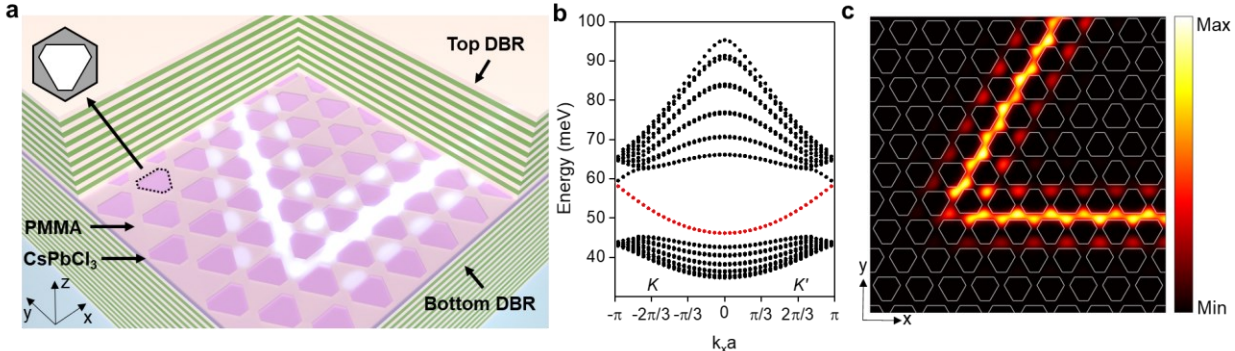
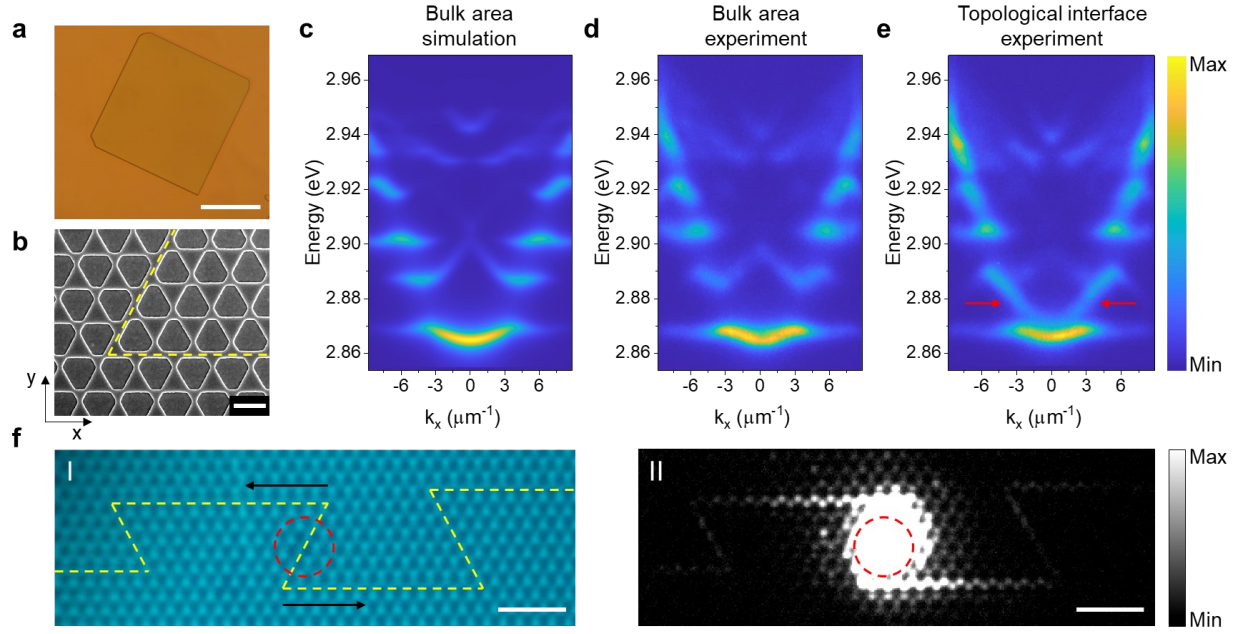


Fig. 1. Schematics and the design of the polaritonic topological valley edge states. a, Schematic illustration of the perovskite microcavity samples. Our perovskite microcavity consists of a single crystal CsPbCl_3 plate and a patterned PMMA spacer sandwiched between the top and bottom distributed Bragg reflector (DBR). The inset in **a** shows the unit cell of the valley Hall crystal. The unit cell consists of a quasi-hexagonal hole (EBL exposed area of PMMA) with two alternating unequal side lengths. By introducing a boundary between domains with opposite hexagonal hole directions, a topological interface with edge states can be formed, as the white highlighted areas shown in **a**. **b**, Projected band structure of the topological interface in a supercell finite in the y direction. The topologically protected valley edge states are confined to the interface, as indicated by the solid red dots. The lattice period is $a = 1.2 \mu\text{m}$. **c**, The real-space polariton density distribution of the topologically protected edge state between two spatial lattice areas. The propagating edge state has a continuous distribution even with a sharp corner of 120° . The details of the simulations of **b** and **c** are shown in Supplementary Text Section I.



1
 2 **Fig. 2. Experimental identification of the topological edge states in polariton lattices.** **a**,
 3 Optical image of a typical large CsPbCl_3 plate transferred onto a bottom DBR substrate. Scalebar
 4 in **a**: 50 μm . **b**, Scanning electron microscope (SEM) image of the fabricated sample before
 5 transferring the top DBR. A topological interface marked by yellow dashed lines are formed by
 6 introducing a boundary between domains with opposite hexagonal hole directions. Scalebar in **b**:
 7 1 μm . **c** and **d**, The simulated and experimental momentum-space dispersions of the bulk area
 8 along the x-axis ($\text{K} \rightarrow \Gamma \rightarrow \text{K}'$ direction), respectively. A large bandgap of 18.8 meV can be
 9 experimentally observed above the ground band in **d**. The dispersion of the bulk area along the y-
 10 axis (ΓM direction) is shown in Extended Data Fig. 7. The dispersions of another sample are shown
 11 in Extended Data Fig. 8. **e**, The momentum-space dispersion of the topological interface along the
 12 x-axis. Compared to the bulk area, topological edge states can be clearly observed, as indicated by
 13 the red arrows. **f**, Robust propagation of the topological edge states. The real-space image of the
 14 waveguide (I) and the saturated PL image of the topological edge state (II) are shown. The dashed
 15 yellow line represents the topological waveguide, and the dashed red circles represent the pumping
 16 laser spot. A bandwidth filter (1-nm full linewidth at half maximum) is used to filter out the
 17 topological edge state (2.881 eV in **e**). The polaritons can clearly propagate across the 120° sharp
 18 corner defects, even with a finite polariton lifetime. Scalebar in **f**: 5 μm .

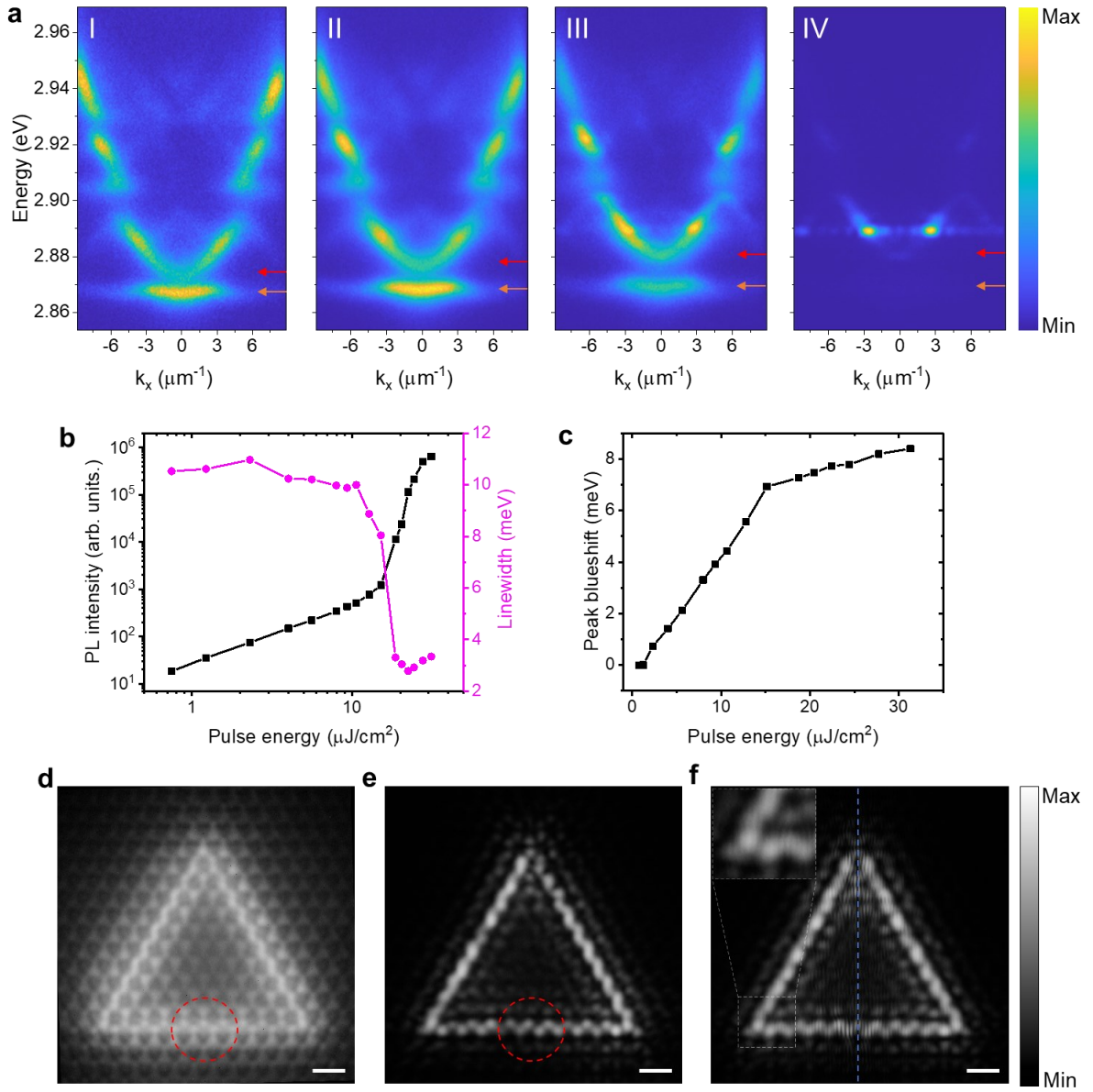


Fig. 3. Room-temperature polariton condensation of the topological edge states. **a-I-IV**, Normalized momentum-space power-dependent PL dispersions of the topological interface along the x-axis at 0.05 P_{th} , 0.5 P_{th} , P_{th} , and 1.5 P_{th} (from left to right, panels I-IV), respectively. P_{th} ($\sim 15.2 \mu\text{J cm}^{-2}$) is the pumping fluence of the condensation threshold. The same sample in Fig. 2d-e is used, but with a larger pinhole in the real-space imaging plane, indicated by the dashed red circles in **d** and **e**, to extract the momentum-space PL. This difference leads to a larger inhomogeneity broadening of the PL spectra in panel **a** compared with Fig. 2d-e. With the pumping power increasing, the topological edge states condensate. The edge states were selectively pumped, thus exhibiting a stronger blueshift compared to the bulk ground state, as shown in **a**. The red and orange arrows indicate the momentum range of the topological edge states.

1 orange arrows in **a** represent the energies of the edge state and the bulk ground state at $k_x = 0$,
2 respectively. **b**, Log-log plot of the integrated PL intensity of the edge state at $k_x = 2.6 \mu\text{m}^{-1}$ and the
3 full width at half maximum (FWHM) versus pulse energy. The nonlinear increase of the PL
4 intensity and the narrowing of the linewidth strongly support the polariton condensation behavior.
5 **c**, PL peak blueshift of the edge state at $k_x = 2.6 \mu\text{m}^{-1}$ versus pulse energy. The repulsive interaction
6 of polaritons induces a continuous blueshift of the topological edge mode. Below the condensation
7 threshold, the primary interaction between polaritons and the exciton reservoir caused a stronger
8 blueshift compared to after the threshold. **d** and **e**, Real-space PL images below and above the
9 condensation threshold, respectively. A spatial light modulator (SLM) created a triangle profile
10 laser beam to pump the topological edge selectively. The red dashed circle area corresponds to the
11 power-dependent data in **(a-c)** by a pinhole in the real-space imaging plane, as shown in Extended
12 Data Fig. 4. Above the condensation threshold, the system condenses at the topological interface
13 in **e**. **f**, The interference of the real-space condensation image in **e** and its mirror image
14 symmetrically overlapped along the blue dashed line. The interference fringes demonstrate the
15 phase-locking and the long-range spatial coherence of the triangular topological edges. The inset
16 shows the zoom-in image of the corner. Scale bars in **(d-f)**: 2 μm .
17

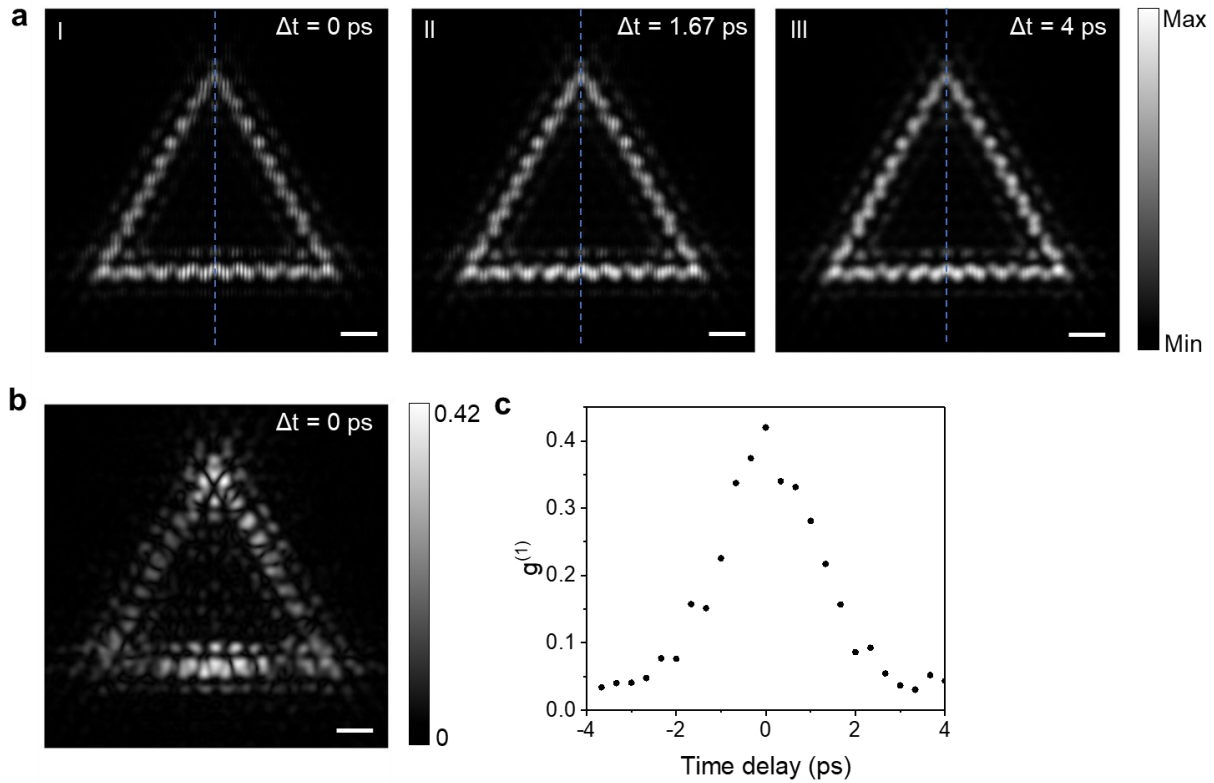


Fig. 4. Characterization of the spatial and temporal coherence of the topological polariton condensation. **a-I-III**, The real-space interference of the condensation at different time delays of 0, 1.67, and 4 ps, respectively. The real-space condensation and its mirror images were symmetrically overlapped along the blue dashed line. **b**, The interference visibility (first-order autocorrelation function $g^{(1)}(r,-r)$) of the real-space interference in **a**-I. The interference visibility is obtained from the interferograms by the Fourier transform. Along the triangle topological interface, the condensation shows good coherence. **c**, Visibility of interference fringe ($g^{(1)}$) at the center of the base of the triangle topological interface as a time delay function. Scale bars in **(a and b)**: 2 μ m.

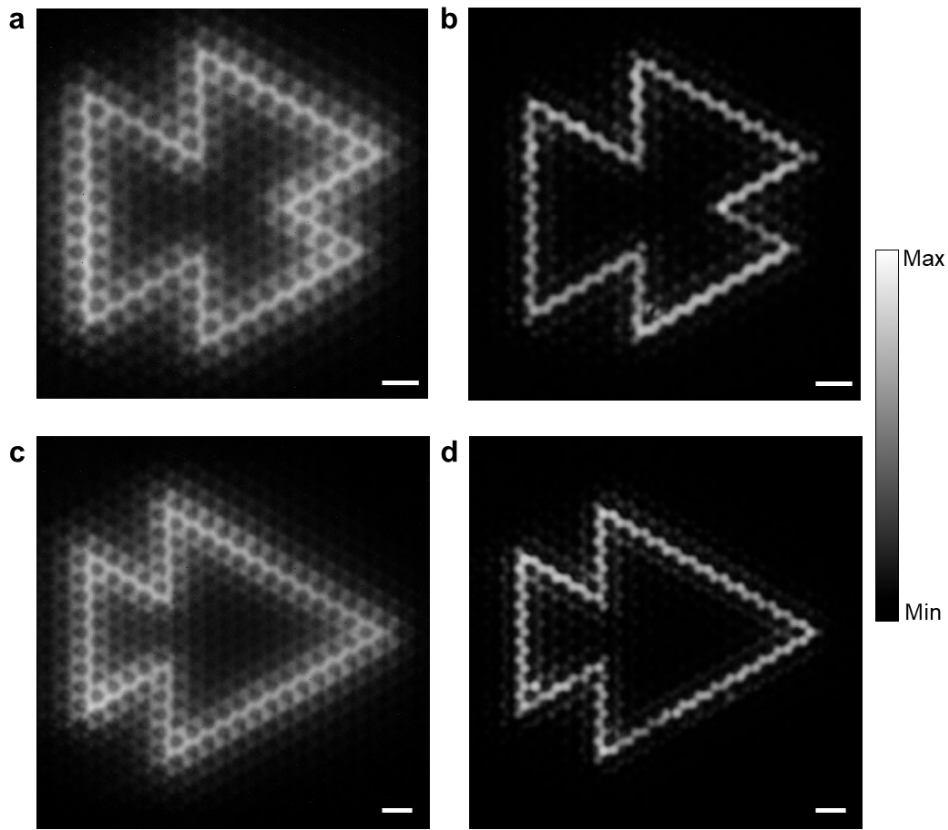


Fig. 5. Room-temperature polariton condensation of the topological edge states with more complex geometries. **a** and **b**, Real-space PL images of an "open-mouth-fish" interface below and above the condensation threshold, respectively. **c** and **d**, Real-space PL images of a "close-mouth-fish" interface below and above the condensation threshold, respectively. Above the threshold, uniform condensations along the topological interfaces can be clearly observed in both cases, proving the potential of our platform to explore the topological phenomena and the applications of topological laser arrays to more intricate geometries. Scale bars in (a-d): 2 μ m.

1 **Methods:**

2 **Fabrication of DBR mirror**

3 For the fabrication of the bottom DBR mirror, 100 nm-thick indium tin oxide (ITO) was first
4 deposited on a quartz wafer to create a charge dissipation layer for electron beam lithography
5 (EBL), followed by the deposition of 15.5 pairs of $\text{SiO}_2/\text{Ta}_2\text{O}_5$ by electron beam evaporation with
6 an advanced plasma source. For the top DBR mirror, 7.5 pairs of $\text{SiO}_2/\text{Ta}_2\text{O}_5$ were deposited on a
7 silicon wafer with 300 nm PMMA by ion-assisted electron beam deposition. The top DBR was
8 picked to a polydimethylsiloxane (PDMS) stamp by resolving the PMMA. All the DBR and ITO
9 layers mentioned above have sharp interfaces and ultra-high flatness.

10 **Synthesis of CsPbCl_3 single crystal microplates**

11 CsPbCl_3 single crystal microplates were grown by solution growth under confinement or chemical
12 vapor deposition (CVD). Samples grown using these two methods exhibit similar optical
13 properties.

14 For solution growth, 0.1 M CsCl and PbCl_2 were dissolved in 1 mL DMSO. The
15 supersaturation solution was filtered and dropped at the edge of the bonded 330-nm DBR
16 nanocavity and 10 min was given until the cavity space was fully filled by the solution through
17 capillary force. Due to the poor solubility of CsCl and PbCl_2 in DMSO, we modified our previous
18 reported method ³⁴ by placing the cavities in a sealed container filled with antisolvent (toluene)
19 vapor to get high-quality CsPbCl_3 single crystals with large size. The toluene vapor will gradually
20 spread into the precursor solution, leading to an increased local solution concentration, which in
21 turn will promote the initiation of perovskite nucleation. The growth process was kept at 50 °C for
22 48 h and then put in a vacuum chamber to eliminate any potential leftover solvent. Finally, the
23 after-growth nanovavity with CsPbCl_3 microplates was opened for devices fabrication.

24 For the CVD growth, 150 μm -thick high-quality muscovite mica substrates were used in CVD
25 growth. In detail, the growth surface of mica was freshly cleaved and placed face-down on the top
26 of a quartz crucible that contained a fine powder mixed with 42 mg CsCl (Sigma-Aldrich; 99.999%
27 purity) and 75 mg PbCl_2 (Alfa Aesar; 99.999% purity). The CVD tube was pumped down and fed
28 with N_2 (99.999% purity) three times after the crucible was sent into the center. Tube pressure was
29 maintained at ambient pressure with an N_2 flow rate of 30 sccm. The system was first heated to
30 575 °C within 30 min, followed by being maintained for 30 min and cooled down to 400 °C within
31 1 h 20 min. After the growth of crystals, the tube was cooled to room temperature naturally.

1 **Fabrication of topological polariton lattice devices**

2 The perovskite plates grown by solution process can be directly used after opening the bonded
3 cavity. The CsPbCl₃ single-crystal microplate grown by as-grown CVD was directly transferred
4 from the mica substrate to the bottom DBR using a standard dry-transfer method. A gentle O₂
5 plasma treatment was used to remove all the residue from the transfer. Then a PMMA spacer layer
6 was spin-coated onto the perovskite microplate, and the topological lattice was patterned via
7 standard EBL with an accelerating voltage of 30 kV, followed by MIBK/IPA 1:3 development of
8 30 s and IPA rinsing of 15 s, respectively. Finally, the top DBR mirror was transferred on top of
9 the PMMA spacer with the topological pattern using a PDMS stamp. The PL of the perovskite
10 microplate shows no noticeable changes after plasma treatment and development (Extended Data
11 Fig. 3). The thickness of the perovskite microplate and the PMMA spacer of the sample in Fig. 2
12 and 3 were 324 nm and 145 nm. Respectively.

13 **Optical measurements of the polariton lattice**

14 The optical measurements of the polariton lattice were performed using a home-built transmission
15 setup at room temperature, as shown in Extended Data Fig. 4a. A 250-fs optical parametric
16 amplifier pulse laser with a repetition rate of 200 kHz was used to achieve non-resonant excitation
17 (370 nm center wavelength). A Hololoye PLUTO reflective liquid-crystal phase-only spatial light
18 modulator (SLM) was used to generate excitation laser patterns. The hologram was computed with
19 a Gerchberg-Saxton algorithm and transferred to an objective (Nikon 40x Plan Fluor ELWD, NA
20 = 0.6) with a Fourier imaging configuration to generate a desired laser pattern on the focal plane.
21 By sampling the intensity of the PL of the perovskites on the triangle pattern, we use feedback
22 methods to adjust the uniformity of the triangle pattern ⁴⁰. A typical PL image with a triangle
23 pumping pattern is shown in Extended Data Fig. 4b. The PL was collected in a transmission
24 configuration. From the other side of the microcavity, another objective (Nikon 40x Plan Fluor
25 ELWD, NA = 0.6) was used to collect the PL. The momentum-space images can be obtained by a
26 Fourier imaging configuration with two achromatic tube lenses. An Andor spectrometer equipped
27 with a 2D EMCCD was used to measure the energy-resolved polariton dispersions. A pinhole was
28 used at the real-space imaging plane to isolate the PL from other areas. A Princeton EMCCD was
29 used to obtain the real-space image. The interference fringe was measured by a CCD camera in a
30 Michelson interferometer.

1 **Data availability:**

2 The authors declare that the main data supporting the findings of this study are available within
3 the paper. Extra data are available from the corresponding authors upon reasonable request.

4 **Acknowledgments:**

5 We thank Dr. Sebastian Klembt and Dr. Ting Cao for the discussions, and A. Gao from SVOTEK
6 Inc. for assisting with the high-quality DBR mirror coating. W. B. thanks the CAREER support
7 from National Science Foundation (award no. DMR-2414131) and the startup support from
8 Rensselaer Polytechnic Institute. W.B., K.P., and W.L. would like to acknowledge support from
9 the Office of Naval Research (award no. N00014-21-1-2099 and N00014-22-1-2322), and support
10 from Nebraska Public Power District through the Nebraska Center for Energy Sciences Research.

11 X.Z. and K.P. thank the support of the Gordon and Betty Moore Foundation (award no. 5722) and
12 the Ernest S. Kuh Endowed Chair Professorship. J.R. and L.G. would like to acknowledge funding
13 from the National Science Foundation (award no. PHY-1847240). Work performed at the Center
14 for Nanoscale Materials, a U.S. Department of Energy Office of Science User Facility, was
15 supported by the U.S. DOE, Office of Basic Energy Sciences, under Contract No. DE-AC02-
16 06CH11357. The research was partly performed in the Nebraska Nanoscale Facility: National
17 Nanotechnology Coordinated Infrastructure and the Nebraska Center for Materials and
18 Nanoscience, supported by the National Science Foundation (award no. ECCS-2025298) and the
19 Nebraska Research Initiative.

20 **Author contributions:**

21 W.B. and K.P. conceived and initiated the project. K.P. performed all optical measurements. W.
22 L. fabricated the microcavities samples with assistance from K.P., C.T., and X.H.. W.L. and K.P.
23 grew and characterized the perovskite materials. M.S., J.R., and L.G. performed all the theoretical

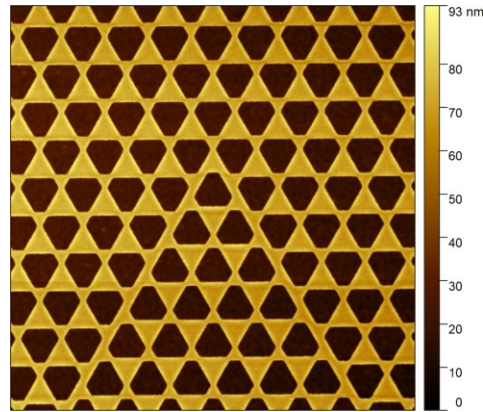
1 analysis and calculations with assistance from K.P.. K.P. and W.B. analyzed all the data. L.G.
2 suggested the initial design. L. Y. provided valuable insight and suggestions. W.B. and X.Z.
3 supervised the whole project. K.P., W. L., M.S., and W.B. prepared the initial draft of the
4 manuscript, and all authors participated in revising the manuscript.

5 **Competing interests:**

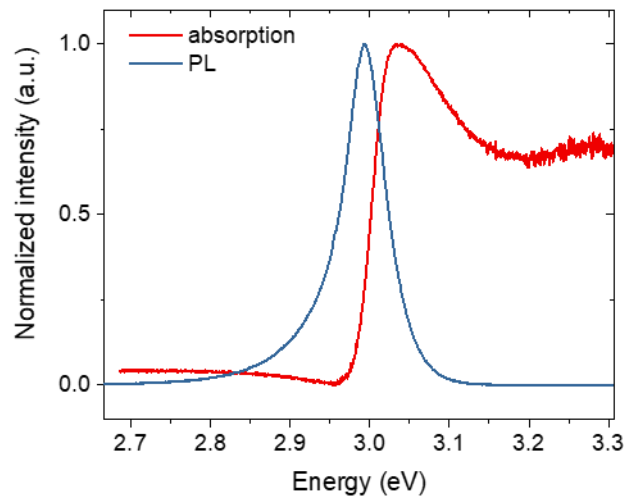
6 The authors declare no competing interests.

7 **Supplementary information:**

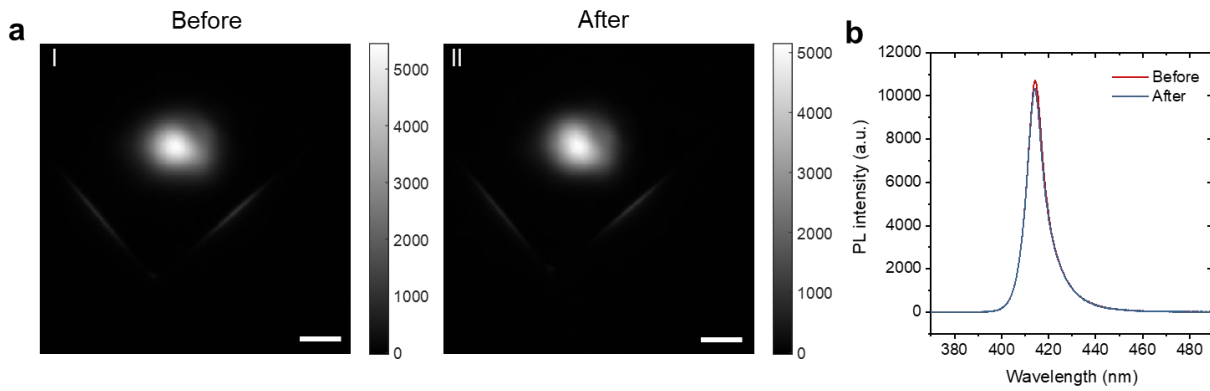
8 Supplementary Information is available for this paper.



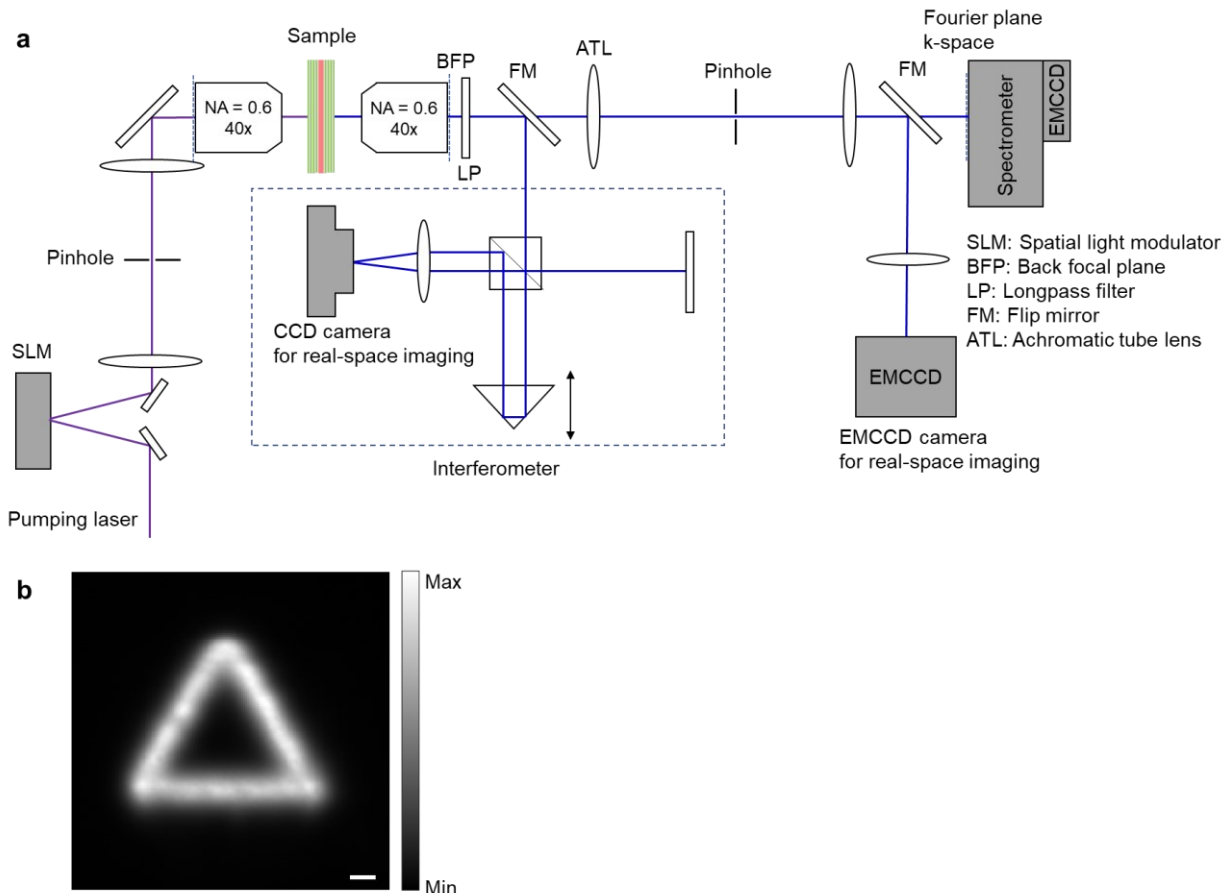
1  0
2 **Extended Data Fig. 1| The AFM image of the patterned PMMA.** For this sample, the PMMA
3 spacer has a thickness of ~70 nm. The topological interface can be clearly observed.
4



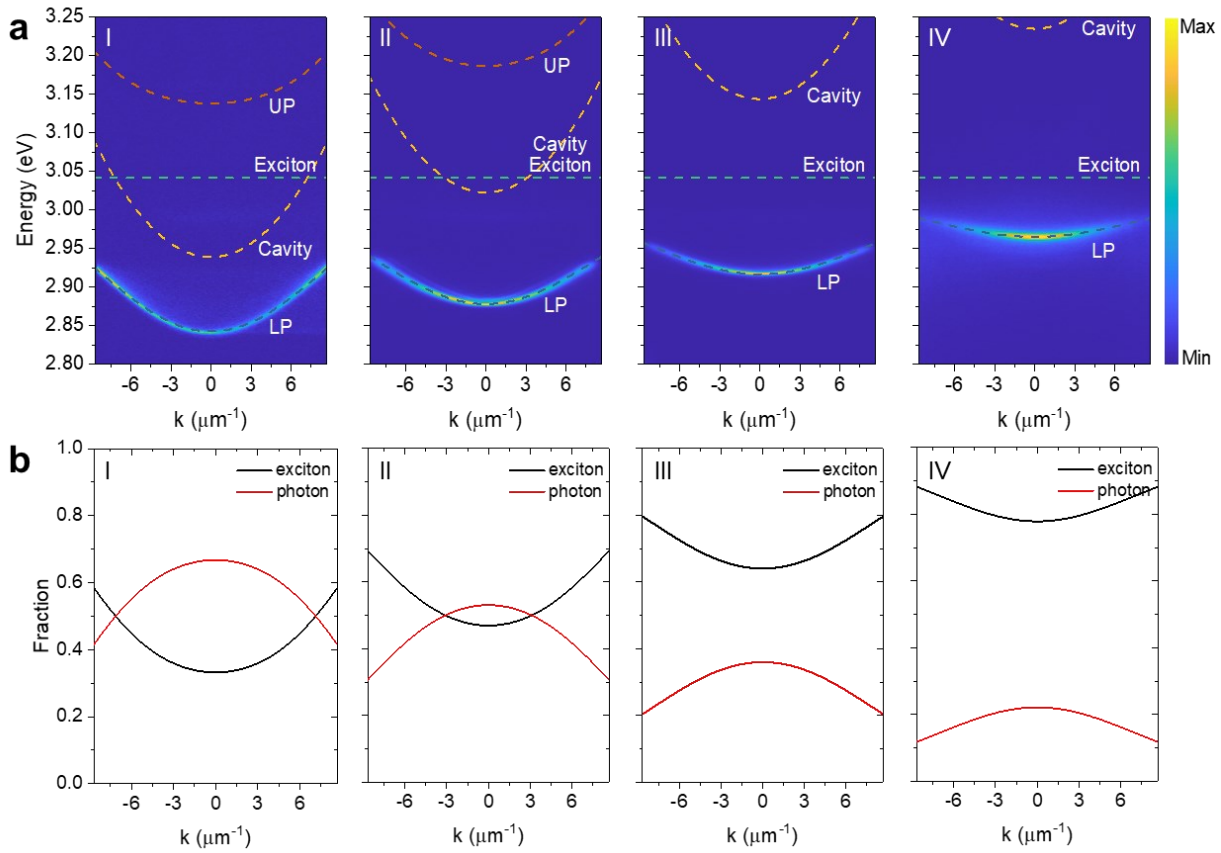
1
2 **Extended Data Fig. 2| Room-temperature absorption and PL spectrum of a CsPbCl_3 Single**
3 **crystal.** The sample shows a strong and stable excitonic absorption peak at room temperature. The
4 corresponding exciton energy peak was extracted as 3.042 eV.
5



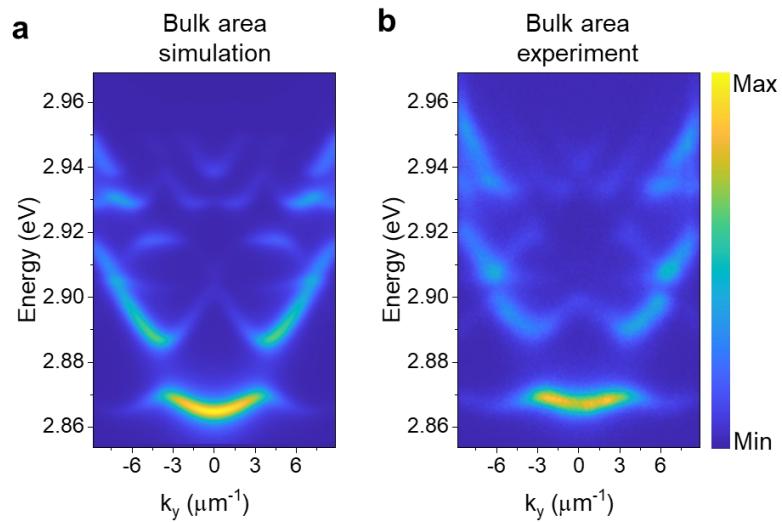
1 **Extended Data Fig. 3| PL spectra of the CsPbCl_3 plate before and after treatments of O_2**
2 **plasma and MIBK/IPA developments.** a-I-II, The real-space images of a single perovskite
3 crystal with non-resonant excitation before and after the treatments of 2 minutes O_2 plasma and 30
4 s soaking in MIBK/IPA and 15 s rinsing in IPA. b, The corresponding PL spectra before and after
5 treatments. Here, after the treatments, the perovskite plate still shows high PL intensity. Scale bars
6 in a: 5 μm .
7



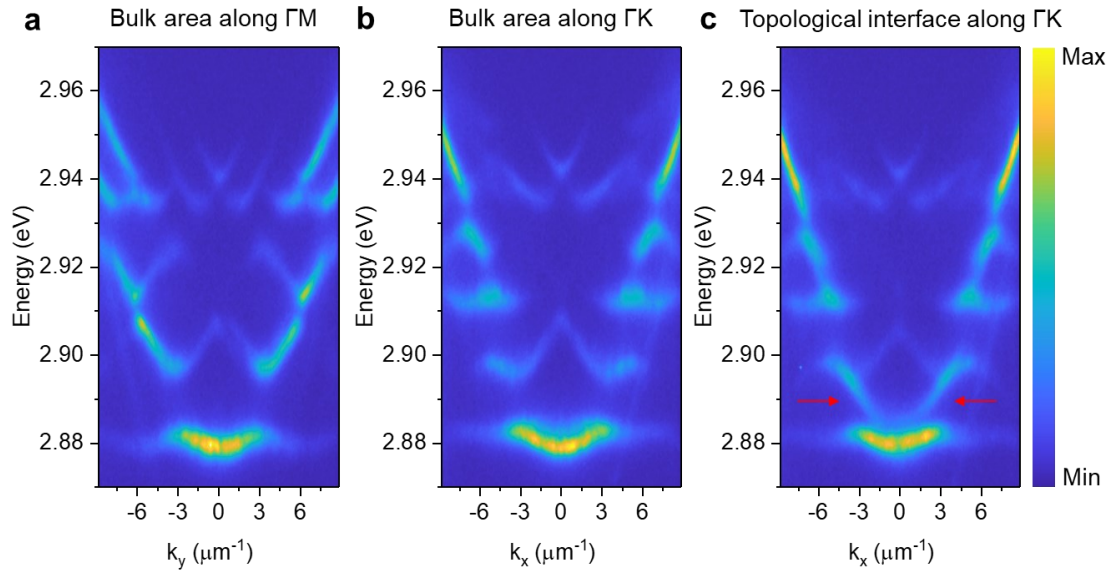
Extended Data Fig. 4| Schematics of the optical measurement setup. **a**, Experimental setup for room temperature polaritonic condensation. A 250-fs optical parametric amplifier pulse laser with a repetition rate of 20 kHz was used to achieve non-resonant excitation (370 nm center wavelength). A reflective liquid-crystal phase-only spatial light modulator (SLM) was used to generate excitation laser patterns. From the other side of the microcavity, another objective (Nikon 40x Plan Fluor ELWD, NA = 0.6) was used to collect the PL. The momentum-space images can be obtained by a Fourier imaging configuration with two achromatic tube lenses. An Andor spectrometer with a 2D EMCCD was used to measure the energy-resolved polariton dispersions. A pinhole was used at the real-space imaging plane to isolate the PL from other areas. A Princeton EMCCD was used to obtain the real-space image. The interference fringe was measured by a CCD camera in a Michelson interferometer. **b**, PL of a bare CsPbCl_3 plate with a triangle pattern pumping. By sampling the PL intensity along the triangle pattern, a feedback method was used to adjust the uniformity of the triangle pattern. Scalebar: 2 μm .



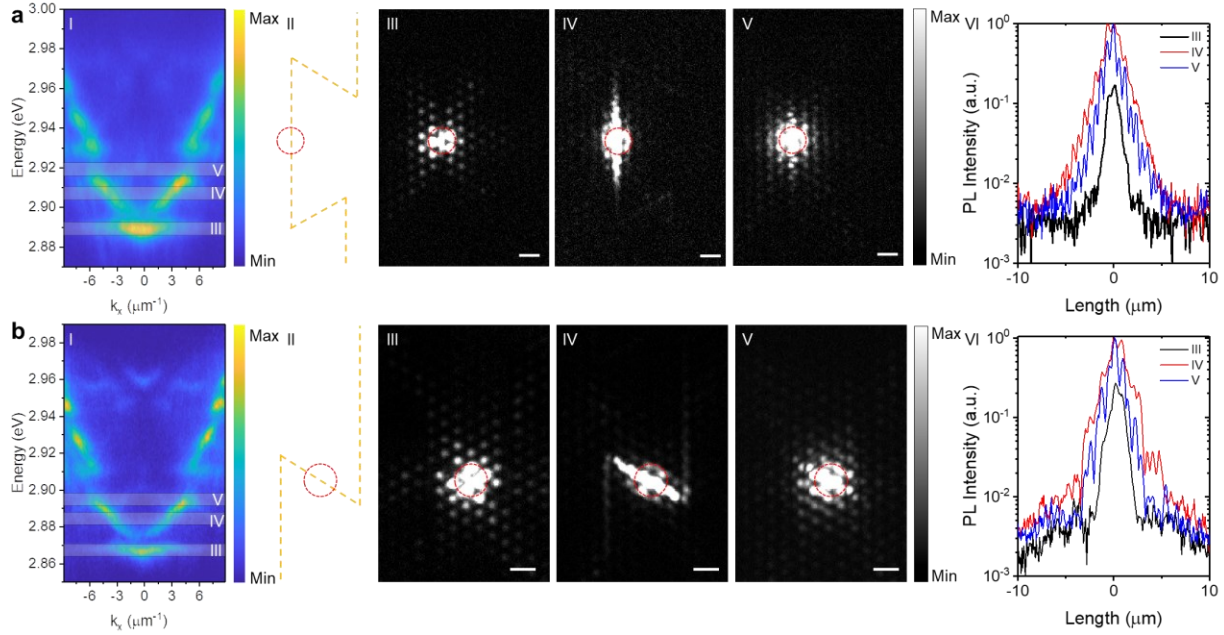
Extended Data Fig. 5| Characterization of the strong coupling behaviors of un-patterned samples. **a-I-IV**, Angle-resolved PL dispersions of un-patterned CsPbCl_3 microcavities. The dashed lines show the fitting curves based on the coupled model in Supplementary Text Section I. Due to variations in the thickness of different perovskite plates and PMMA coatings, these samples show different strong-coupling behaviors. Here, the exciton energy was extracted from the absorption spectrum in Extended Data Fig. 2 as $E_{\text{ex}} = 3.042$ eV. The cavity effective mass is fitted as $m_{\text{cp}} = 0.11 \text{ meV}/(\mu\text{m}/\text{ps})^2$ for these four cavities, corresponding to a same refractive index for these perovskites. With detuning change from negative to positive (-103, -19, 97, and 193 meV from I-IV, respectively), the bending effect of the lower polariton branch demonstrates the strong coupling behavior clearly. Due to the strong absorption and large coupling strength, the upper polariton branch cannot be observed. All the lower polariton branches show negligible TE-TM splitting. **b-I-IV**, The corresponding Hopfield coefficients of the lower polariton branches based on the strong coupling model. On the other hand, due to the large Rabi splitting strength, the lower polariton branch can condensate with a large range of fractions of exciton and photon.



Extended Data Fig. 6| The momentum-space dispersions along the y-axis. **a** and **b**, The simulated and experimental momentum-space dispersions of the bulk area along the y-axis (Γ M direction) of the sample in Fig. 2d of the main text, respectively.

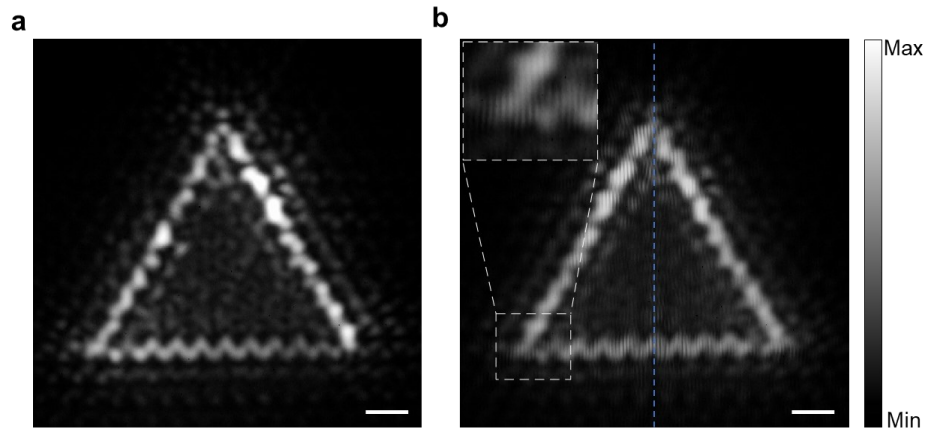


Extended Data Fig. 7| The momentum-space dispersions of another sample. a and b, The PL dispersions of the bulk area along Γ M and Γ K directions, respectively. An energy gap of 14.3 meV was observed in this sample. **c,** The dispersion of the topological interface area along Γ K direction. The topological edge states are observed clearly, as indicated by the red arrows.



Extended Data Fig. 8| Energy-resolved polariton propagation of two waveguide samples. **a**-I, The PL dispersion of the topological interface along the x-axis ($K \rightarrow \Gamma \rightarrow K'$ direction). A non-resonant laser (dashed red circle) was used to pump the Ω -shaped waveguide, as shown in II. A bandwidth filter (1-nm full linewidth at half maximum) is used to extract polariton PL below, within, and above the topological bandgap, as indicated by the semi-transparent rectangle in a-I. The corresponding saturated real-space propagations are illustrated in the Fig. a-III, a-IV, and a-V, respectively. Only the topological edge state within the topological bandgap in a-IV can propagate along the Ω -shaped waveguides robustly. Comparatively, the bulk state in a-III lacks eigenstates on the interface, leading to undirected diffusion. In a-V, although there are trivial edge states above the topological band gap, the strong decay occurs when polaritons encounter 120° sharp corners due to the lack of topological protection. This is also illustrated by the normalized PL intensity in a-VI. Due to the maximum PL being in the bulk state in III, the PL intensity on the waveguide is lower than that of the edge states, as shown by the solid black line in Fig. a-IV. There are still some bulk states in a-V because we can only filter the PL signal by a bandwidth filter. It is worth noting that, different from the passive silicon-based waveguides with negligible losses, in our active perovskite microcavity, before polariton condensation, strong absorption from the perovskite gain medium impedes the long-distance propagation of polaritons. A Z-shaped waveguide in another sample also shows similar results in **b**. These different propagations are also proved by the time-dependent numerical simulations (described in Supplementary Text Section III

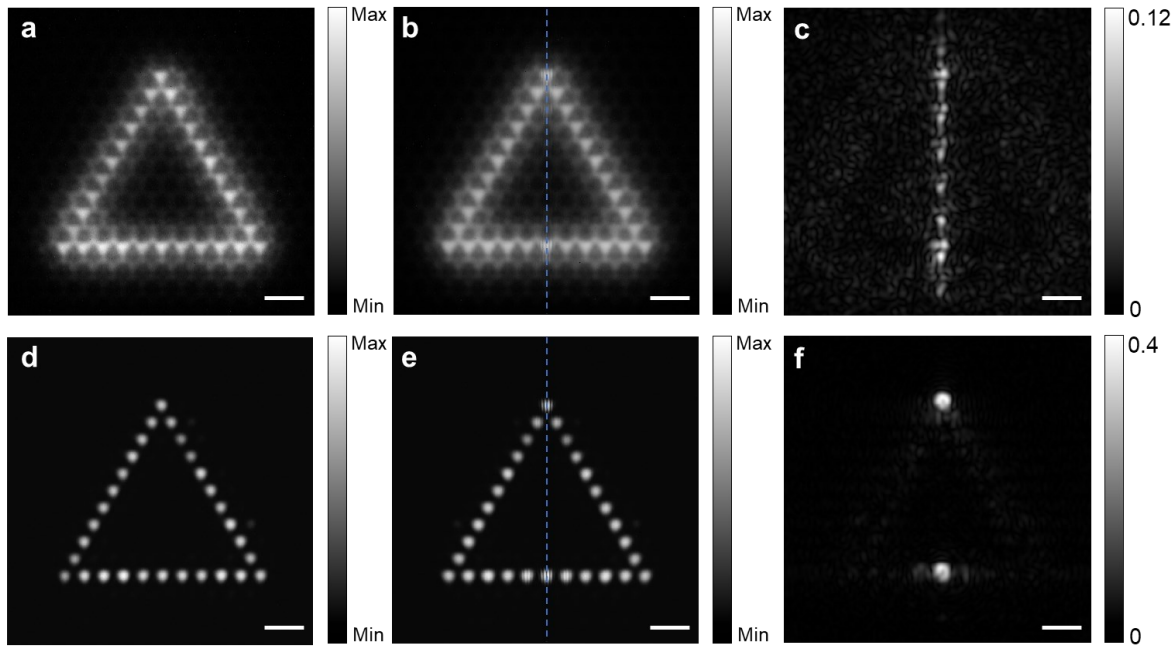
1 and Supplementary Videos S1-S3). These results prove the robust topological propagation of the
2 edge state in our perovskite polariton system. Scale bars in **(a** and **b**): 2 μ m.



1

2 **Extended Data Fig. 9| Another sample for room-temperature polariton condensation of the**
 3 **topological edge states.** **a**, Real-space PL image above the condensation threshold. A triangle
 4 laser profile was used to pump the topological edge selectively. Above the condensation threshold,
 5 the system condensates at the topological interface. **b**, Interference of the real-space lasing image
 6 in **a** and its mirror image. For this sample, even with some defects and clearly noticeable
 7 inhomogeneity, the interference fringes still demonstrate the phase-locking and the long-range
 8 spatial coherence of the entire triangle topological edge. The inset shows the zoom-in image of the
 9 corner. Scale bars in **(a and b)**: 2 μ m.

10



Extended Data Fig. 10 | Room-temperature polariton condensation of the trivial bulk states.

a, Real-space PL image below the condensation threshold. A triangle laser profile was used to pump the bulk area. The real-space image and its mirror image were symmetrically overlapped along the blue dashed line. Below the condensation threshold, only short-range interference near the symmetry axis was observed in **b**. **c**, the extracted first-order autocorrelation function $g^{(1)}(r,-r)$ from **b**. **d**, Real-space PL image above the condensation threshold. The condensation occurs at the ground bulk state. Because of the non-propagation character, this bulk condensations act like isolated condensates and no long-range spatial coherence of the entire triangle pumping area was observed in the interference image (**e**) and the extracted interference visibility (**f**). Scale bars in (**a-f**): 2 μ m.